ATLAS NOTE

ATL-PHYS-PUB-2016-015

2nd August 2016

Electron and photon energy calibration with the ATLAS detector using data collected in 2015 at $\sqrt{s} = 13$ TeV

The ATLAS Collaboration

Abstract

This document describes the calibration of the energy of electrons and photons, as implemented by the ATLAS experiment for proton-proton collision data collected in 2015 and the first part of 2016 at $\sqrt{s} = 13$ TeV. The strategy adopted was developed during LHC Run-1 and is based both on simulations and on data collected during 2015. The steps of the calibration scheme based on simulation have been fully re-optimised using the updated detector description and reconstruction procedures. The data-driven corrections have been re-evaluated or extrapolated from Run-1 results, in the cases where the amount of data collected in 2015 was insufficient. The uncertainty model has been updated in order to include these extrapolation uncertainties.

ATL-PHYS-PUB-2016-015
02/08/2016

1 Introduction

A precise knowledge of the energy scale and resolution of prompt electrons and photons is an important ingredient in most physics analyses, in particular in the case of precision measurements. This document presents the energy calibration used by the ATLAS experiment [1] for the analyses in Run-2 in the central region ($|\eta| < 2.47$). The calibration is based both on simulations and real data and follows the calibration scheme used in Run-1 based on proton-proton collisions at $\sqrt{s} = 8$ TeV [2] collected in 2012. The main calibration corrections and their related systematic uncertainties have been updated, using the integrated luminosity of 3.2 fb^{-1} collected in 2015 for proton-proton collisions at $\sqrt{s} = 13$ TeV. The new simulation (MC) samples account for changes in the reconstruction of electrons and photons, and include an updated description of the detector. The most significant of these updates is the introduction of the new innermost layer, the *Insertable B-Layer* (IBL) [3], in the pixel detector, with the goal of improving the tracking performance at the higher luminosities and energies during Run-2 operation and beyond.

The energy calibration scheme can be summarised in three main steps:

- data-driven corrections optimised to mitigate the non-uniformity in detector response (applied only to data);
- simulation-based calibration (applied to data and simulation);
- data-driven corrections with energy scale factors (applied to data) and correction of the resolution (applied to simulation).

Since the dataset available so far is still statistically limited with respect to the one used in Run-1, not all the data-driven corrections can be re-evaluated with suitable accuracy. In such cases the corrections measured in Run-1 are used, with increased systematic uncertainties in order to account for the extrapolation to Run-2 conditions.

This document summarises what has been updated with respect to the previous calibration as follows. First, in Section 2, the reconstruction of electrons, photons and of their energy is summarised; Section 3 shows the updated simulation-based calibration; Section 4 illustrates the measurement of the energy scales and the correction to the resolution with $Z \to ee$ events at $\sqrt{s} = 13$ TeV; finally Section 5 summarises the updates to the uncertainty model.

2 Electron and photon reconstruction and calibration procedure

The reconstruction of electrons, photons, and of their energies relies on the measurements of electromagnetic showers in the electromagnetic calorimeter (ECAL). This is briefly summarised below, focusing on the changes introduced in Run-2. More details can be found elsewhere [2].

The raw signal from each calorimeter cell is amplified, shaped and sampled. To support higher trigger rates, suitable for Run-2 conditions (higher instantaneous luminosity and centre of mass energy), the number of samples used was decreased from five to four. The amplitude of the sampled signal is evaluated using a set of *optimal filter coefficients* which was re-optimised for the new sampling and the 25 ns bunch spacing of the proton beams. The digitised samples are then converted into the energy deposited in the cell using a hardware calibration periodically updated during the data-taking period.

The reconstruction of electrons and photons in the central region ($|\eta| < 2.47$) starts from energy deposits (clusters) in the ECAL. Differently from the reconstruction used in Run-1 all the electromagnetic particles are reconstructed with the same cluster size; in the barrel a cluster size corresponding to 3×7 cells in the middle layer is used (equivalent to an area of size $\Delta\eta \times \Delta\phi = 0.075 \times 0.175$), while a cluster of 5×5 cells in the middle layer is used in the endcaps (equivalent to an area of $\Delta\eta \times \Delta\phi = 0.125 \times 0.125$). The increase of the cluster size for unconverted photons in Run-2 in the barrel allows to harmonize the reconstruction of electrons and photons in order to minimize the uncertainty due to the extrapolation of the response between electrons and photons.

Tracks reconstructed in the inner detector, loosely matched in space to the ECAL clusters, are selected, requiring a minimum number of hits in the pixel and overall silicon layers. The classification of the electromagnetic particles is driven by the presence of matched tracks. If no tracks are associated to an ECAL cluster it is classified as an "unconverted photon". In case the cluster is matched to a pair of oppositely-charged tracks, collinear at the production vertex and compatible with electrons in the transition radiation tracker detector (TRT), the cluster is considered as a "converted photon". Since the detection of conversion track pairs becomes inefficient at large conversion radius, a cluster matched to one track can also be considered as a converted photon: to discriminate from electrons produced at the interaction point, the track must have no hits in the innermost layers of the pixel detector.

Uniformity corrections are applied to data to equalise the response of the longitudinal layers of the ECAL between data and simulation. They have been derived using data in 2012 and are used in Run-2. The validity of these corrections has been checked using data from 2012 reprocessed under the conditions of 2015 (for example using four rather than five time samples to determine the energy deposited in each cell). Other corrections, such as geometric effects are applied using the values derived in Run-1. The correction due to non-nominal high-voltage regions has been updated with the Run-2 configuration.

A multivariate regression algorithm calibrates the energy of electromagnetic particles correcting for the energy deposited in front of the calorimeter (typically between a few percent and 20% of the electron energy for 100 GeV energy electrons [1]) and outside of the cluster (around 5%), as well as for the variation of the energy response as a function of the impact point on the calorimeter. The update of this algorithm is described in the next section.

Finally, in order to account for any residual disagreement between data and simulation, the energy scale of electrons is extracted using $Z \to ee$ events through an in-situ procedure described in Section 4.

3 Monte Carlo based calibration

The Monte Carlo based calibration has been updated using single particle simulations without pileup with the latest simulation and reconstruction algorithms. The calibration is based on a multivariate boosted decision tree with gradient boosting. Some improvements have been introduced, in particular in the transition region between the barrel and the endcap.

The list of input variables has been updated by replacing the longitudinal shower depth with the ratio of the values of the energy measured in the first two layers of the calorimeter E_1/E_2. This variable is very correlated with the longitudinal shower depth but it has been studied in more details comparing data with simulations. The pseudorapidity region covered by the calibration has been extended to cover the region $|\eta| \in [0, 2.5]$, including the transition region between the barrel and the endcap of the electromagnetic calorimeter. In this region, $1.4 < |\eta| < 1.6$, the amount of material traversed by the particles before

reaching the first active layer of the calorimeter is quite high (from 5 to almost 10 radiation lengths) and the energy resolution is very degraded. To mitigate this effect the energy measured by the E4 scintillators installed in the transition region has been introduced as an additional variable to the training of the calibration. The E4 scintillators are part of the Intermediate Tile Calorimeter (ITC). The ITC is located in the gap region, in between the long and the extended barrels of the Tile Calorimeter and it has been designed to correct for the energy lost in the passive material that fills the gap region. Electrons and photons in the gap region deposit energy in the barrel and the endcap of the electromagnetic calorimeter and in the E4 scintillators as well.

Figure 1 shows the improvement in the energy calibration in the region $1.4 < |\eta| < 1.6$ for electrons, converted and unconverted photons with generated energy between 50 and 100 GeV evaluated using single particle simulations without pileup. The width of the distribution of the ratio of the calibrated energy E_{calib} to the generated energy of the particle E_{gen} has been estimated using a Gaussian fit of the core of the distribution and using the interquartile range (IQR, the difference between the third and the first quartile). In the first case the improvement in the energy resolution is about 20% for electrons, 15% for converted and 8% for unconverted photons when comparing to a similar calibration without using the information from the scintillators and 22%, 20% and 29% respectively when using the IQR.

A dedicated systematic uncertainty has been introduced to take into account the energy scale of the scintillators and it has been propagated to the final calibrated energy as described in Section 5.2.

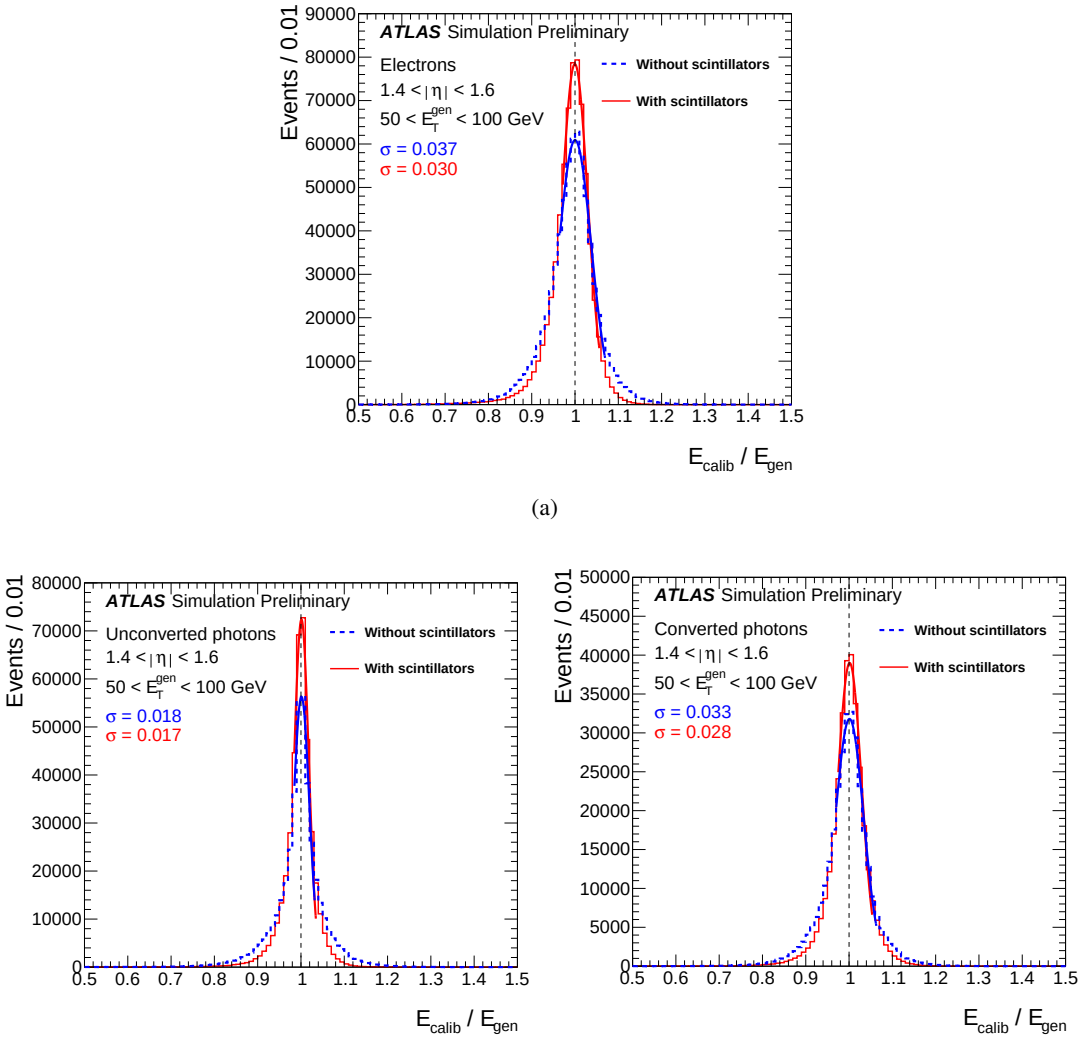

Figure 1: Distributions of the calibrated energy, E_{calib}, divided by the generated energy, E_{gen}, for (a) electrons, (b) unconverted photons, and (c) converted photons, generated with $1.4 < |\eta| < 1.6$ and $50 < E_{\text{T}}^{\text{gen}} < 100\,\text{GeV}$. The dashed (solid) histogram shows the results based on the energy calibration without (with) the scintillator information. The curves represent Gaussian fits to the cores of the distributions, between [-1, +2] standard deviations, and provide the results shown for the observed resolutions σ.

4 In-situ corrections

After the application of the corrections for the non-uniformity of the detector response and of the simulation-based calibration, a residual disagreement in the energy scale and resolution may be present between data and simulation. In order to correct this residual mismatch an in-situ procedure, developed in Run-1 (see sec. 9 of [2]), is applied. The energy mis-calibration is defined as the difference in response between data and simulation, and is parametrised as

$$E_i^{\text{data}} = E_i^{\text{MC}}(1 + \alpha_i) \tag{1}$$

where E_i^{data} and E_i^{MC} are the electron energies in data and simulation, and α_i represents the deviation from optimal calibration, in a given pseudorapidity region labeled i.

The relative energy resolution is parametrised as

$$\frac{\sigma(E)}{E} = \frac{a}{\sqrt{E}} \oplus \frac{b}{E} \oplus c \tag{2}$$

where a is the *sampling term* related to shower fluctuations in the calorimeter and modeled by simulation, b is the *electronic noise term* measured in calibration runs, and c is the *constant term*.

The difference in energy resolution between data and simulation, which does not to first order depend energy, can be modeled by an additional effective constant term (c_i'):

$$\left(\frac{\sigma(E)}{E}\right)_i^{\text{data}} = \left(\frac{\sigma(E)}{E}\right)_i^{\text{MC}} \oplus c_i' \quad , \tag{3}$$

for a given pseudorapidity region.

Energy scale corrections (α_i) and additional constant terms for the energy resolution (c_i') have been estimated, through a *template* procedure, using $Z \to ee$ events selected in the 2015 data sample.

The sources of systematic uncertainty for this procedure can be grouped in three categories:

- event selection:
  - selection criteria for the candidate electrons (identification, isolation and energy loss);
  - differences in the efficiency of electron selection criteria between data and simulation;
  - selection criteria for the candidate Z;
  - evaluation of the impact of the electroweak background ($Z \to \tau\tau$ and $t\bar{t}$) - the Run-1 estimate for this uncertainty has been adopted;
- calibration procedure:
  - methodology (different strategies for the extraction of α_i and c_i' parameters);
  - closure;
- material:
  - mis-modeling of the material for the IBL in the simulation.

The measured values are reported in Figure 2, along with the total systematic uncertainty of the in-situ calibration procedure. These corrections are applied both to electrons and photons.

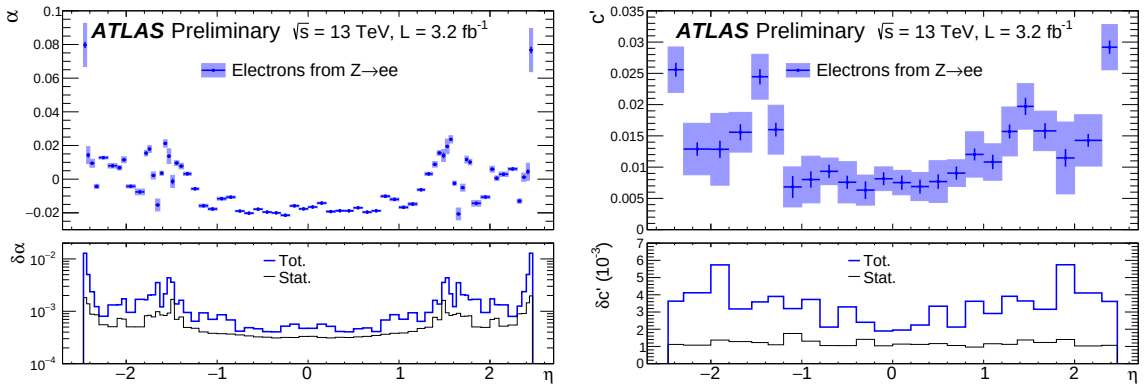

(a) (b)

Figure 2: (a) Energy scale factor α and (b) additional constant term c' for energy resolution from $Z \to ee$ events as a function of η. The uncertainty bands on the top plots represent the total uncertainties on these quantities, while the thin black (resp. thick blue) lines at the bottom represent the statistical (resp. total) uncertainties.

5 Uncertainties on energy scale and resolution

In addition to the uncertainties discussed in Section 4 for the in-situ corrections, many additional sources of uncertainty on the energy scale and resolution for electrons and photons are considered: beam configuration, detector description, procedures and statistics of the samples used for data-driven corrections. A detailed analysis of all those sources was performed in Run-1 for precision measurements (Section 10 of [2]). The same model has been implemented for the Run-2 calibration with the updates described in the following.

Since the uncertainty model developed in Run-1 accounts for more than 70 independent systematic variations for the energy scale, a simplified model has been developed, considering all the effects to be fully correlated across η, and summing the effects of all sources of systematic uncertainty in quadrature to form a single systematic variation. This systematic model is usually pessimistic and is used only by analyses not very sensitive to the energy scale of electrons and photons. A similar simplification for the uncertainties on the resolution is provided.

The values of most of the systematic uncertainties have been taken from Run-1 results. Section 5.1 lists the checks and the updates regarding the most important uncertainties with respect to the uncertainties used in Run-1, while Section 5.2 shows the uncertainty on the energy scale arising from the introduction in the calibration of the scintillators in the region $1.4 < |\eta| < 1.6$, as described in Section 3.

5.1 Main sources of uncertainty in Run-2

The main sources of uncertainty on the energy scale and the ones that have been updated are shown in Figure 3 for $|\eta| < 0.6$ and $5\,\text{GeV} < E_{\text{T}} < 1\,\text{TeV}$ for electrons, unconverted and converted photons, including

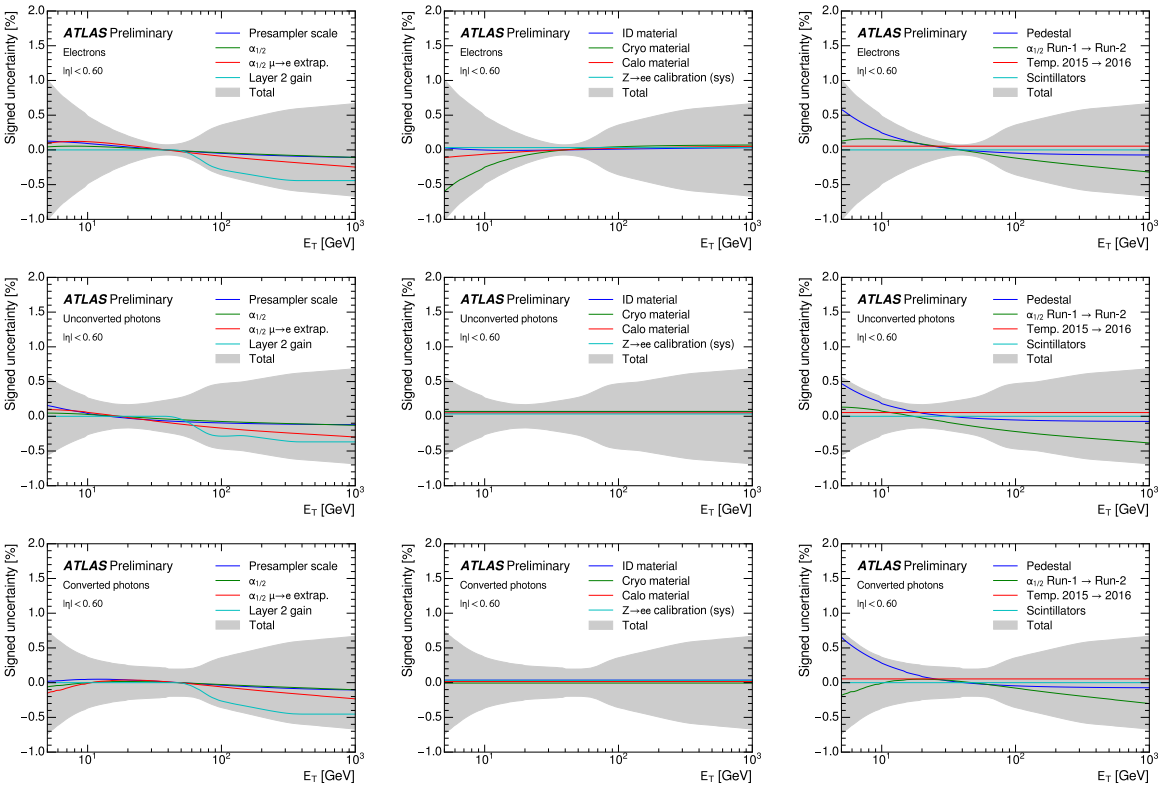

Figure 3: Main contributions to the systematic uncertainty on the energy scale after calibration corrections, shown as a function of E_{T} and for $|\eta| < 0.6$, in the case of electrons (top row), unconverted photons (middle row), and converted photons (bottom row). The total uncertainty bands represent the quadratic sum of all systematic uncertainty sources described in the text and represented in the various columns. The last column in particular shows the additional systematic uncertainties introduced from Run-1 to Run-2 and the temperature uncertainty added when comparing 2015 data to 2016 data.

- *Presampler*: the uncertainty on the calibration of the thin presampler layer is not expect to be changed in Run-2 with respect to Run-1. The presampler covers the pseudorapidity interval $|\eta| < 1.8$, and is used to correct for energy loss upstream of the calorimeter.
- *Layer intercalibration*: the scale factors $\alpha_{1/2}$ used to intercalibrate the first two layers of the electromagnetic calorimeter as a function of η have been checked using the 2015 dataset, and found to be in good agreement with the measurement using the 2012 dataset. An additional systematic uncertainty equal to the maximum observed discrepancy ($\sim$ 1.5%) has been included in the uncertainty model. The same uncertainty relative to the *muon to electron extrapolation* evaluated for Run-1 has been considered for Run-2.
- *Layer 2 gain*: the dependence of the energy response from the gain used in the readout chain has been studied in Run-1, and the relative uncertainty has been retained.
- *Material*: the values of the uncertainties relative to the description of the material before the calorimeter for $|\eta| < 2.5$ have been retained from the data driven studies in Run-1. An additional source of uncertainty for the mis-modeling of the IBL material in the simulation has been

considered for Run-2, and its effect has been evaluated in the frame of the in-situ calibration (Section 4).

- *In-situ calibration ($Z \rightarrow ee$)*: the uncertainty on the scale and additional constant term have been re-evaluated using 2015 dataset, as described in Section 4.
- *Pedestal*: in 2012 data residual small baseline shifts (±10 MeV) were observed in data and an effect coming from the pedestal determination in electronics calibration data has been corrected as a function of the bunch train position. Nevertheless residual effects from pileup induced shifts can be present after the correction, and given the higher expected luminosity in Run-2, this systematic uncertainty has been estimated to be ±20 MeV.
- *Pileup and temperature*: the in-situ calibration procedure accounts for any possible difference in pileup and temperature conditions between data and simulation for 2015 data. In order to account for differences between 2015 and 2016 datasets in pileup conditions, an uncertainty of 0.02% has been added to the uncertainty model. Similarly an uncertainty of 0.05% has been added to account for temperature difference of the liquid argon between 2015 and 2016 (from test beam studies the signal in the ECAL shows a -2%/K dependence due to density and drift velocity variations [4]).

5.2 Uncertainties related to the scintillators for $1.4 < |\eta| < 1.6$

As described in Section 3, the simulation-based calibration has been extended to the transition region between the barrel and the endcap of the electromagnetic calorimeter. Four independent sources of uncertainty on the response of the scintillators have been considered:

- data-simulation difference evaluated as the difference in the mean of the energy in the scintillators in $Z \rightarrow ee$ events: it ranges between 1% and 4.3%, depending on η. This is mainly due to the modeling of the light attenuation inside the scintillators;
- uncertainty on the electromagnetic scale calibration factor that converts the Tile Calorimeter signals to the energy deposited by electrons. From studies of the Tile Calorimeter in test-beam [5] this factor has a spread of 2.4% which has been taken as an uncertainty;
- initial intercalibration using the Minimum Bias (MB) system: 1%;
- uncertainty of the calibration using laser over the whole year: 4%.

The last two sources of uncertainty correspond to the time-dependent calibration of the responses of the E4 scintillators. The monitoring and calibration of E4 scintillators response are performed by two different calibration systems: a Laser system [6] that provides the calibration of the photomultipliers gain and the MB system [7] that is capable to monitor and calibrate E4 scintillators responses based on the integrated currents from minimum bias events over time during data-taking. Initial intercalibration of all E4 scintillators in the first 25 ns collision run was performed by the MB system with 1% uncertainty and after that, during data-taking only the laser was used. Those systematic effects are considered independent, and added in quadrature in the *Scintillators* uncertainty.

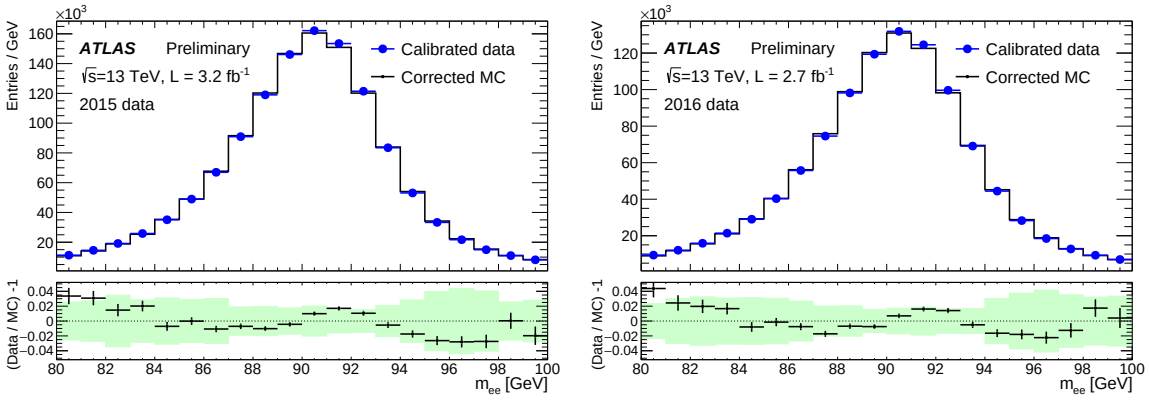

(a) (b)

Figure 4: Electron pair invariant mass distribution from $Z \to ee$ decays in data compared to simulation after the application of the full calibration, for (a) 2015 dataset and (b) a subset of 2016 dataset. The distributions for the data are shown without applying any background subtraction. The simulation is normalised to data. The bottom panels show the residuals for the data/MC ratios together with the total uncertainty (shaded green band).

6 Calibration checks

In order to check the accuracy of the whole calibration procedure, the electron pair invariant mass (m_{ee}) distribution of $Z \to ee$ candidates, is compared between data and simulation. Figure 4 shows the comparison separately for the 2015 dataset (3.2 fb^{-1} of integrated luminosity) and for the first part of the 2016 dataset (2.7 fb^{-1} of integrated luminosity). These comparisons are performed without applying any mass-dependent background subtraction to the data: the multi-jet contributions is evaluated to be negligible and the contribution from other non-resonant processes ($Z \to \tau\tau$ and $t\bar{t}$) is evaluated to be $\sim$ 1.5% for m_{ee} = 80 GeV [8]. Data and simulation agree within uncertainties for both datasets.

The instantaneous luminosity delivered by the LHC has largely increased during 2015 and 2016, and the average number of simultaneous interactions per bunch crossing μ has increased from 13.6 for 2015 to 20.5 for the initial 2016 dataset shown in this note. Because of this large change in the data-taking conditions, the stability of the calibration has been studied as a function of μ and of time in both datasets. Figure 5 shows the ratio of the invariant mass from $Z \to ee$ events to the average value observed in the whole 2015 data sample ($\langle m_{ee}(2015)\rangle$) as a function of μ and time for both datasets. The stability of the response of the electromagnetic calorimeter versus μ and time is seen to be better (at most 0.1%) than the current systematic uncertainty of the calibration procedure.

7 Conclusions

The calibration of electrons and photons described in [2] has been updated to take into account the upgrade of the detector, the updates and improvements of the simulation, the reconstruction and data-taking conditions using new simulated samples and 3.2 fb^{-1} of data at $\sqrt{s}$ = 13 TeV collected during 2015. In particular, an updated simulation-based calibration has been provided and energy scale factors and additional contributions to the energy resolution have been obtained from $Z \to ee$ events. The layer calibration estimated from Run-1 is still used, but its validity has been checked and an additional systematic

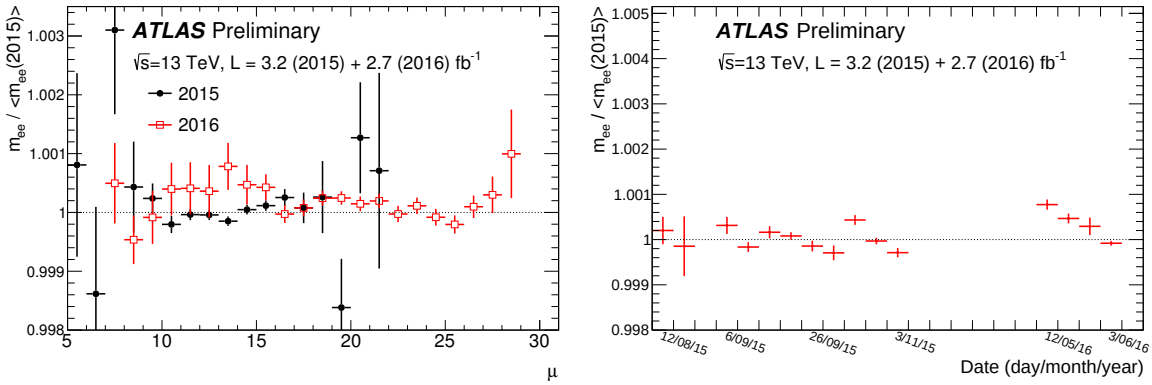

(a) (b)

Figure 5: Stability of the average value of the electron pair invariant mass for $Z \to ee$ events (a) as a function of the average number of interactions per bunch crossing, μ, and (b) as a function of the time of data taking using data collected in 2015 and 2016. Each bin shows the average invariant mass divided by the average invariant mass measured in 2015.

uncertainty has been introduced to account for the changes observed from Run-1 to Run-2. The corrections for the non-nominal HV-corrections have been updated. Additional systematic uncertainties for the different pileup conditions between Run-1 and Run-2 and between 2015 and 2016 have been added. Owing to a small difference in the temperature of the LAr between 2015 and 2016, an additional systematic uncertainty on the energy scale has been introduced for 2016.

In summary, the energy scale for electrons from $Z \to ee$ decays has been obtained with uncertainties between less than one per mil in the barrel and a few per mil in the endcaps. The uncertainty on the effective constant term added to the simulation is between two and five per mil. The stability of the energy response versus the number of interactions per bunch crossing and versus time has been verified to be better than the per mil level.

References

[1] ATLAS Collaboration, *The ATLAS Experiment at the CERN Large Hadron Collider*, JINST **3** (2008) S08003.

[2] ATLAS Collaboration, *Electron and photon energy calibration with the ATLAS detector using LHC Run 1 data*, Eur. Phys. J. C **74** (2014) 3071, arXiv: 1407.5063 [hep-ex].

[3] ATLAS Collaboration, 'ATLAS Insertable B-Layer Technical Design Report', tech. rep. CERN-LHCC-2010-013. ATLAS-TDR-19, CERN, 2010, URL: https://cds.cern.ch/record/1291633.

[4] 'ATLAS liquid-argon calorimeter: Technical Design Report', Technical Design Report ATLAS, CERN, 1996, chap. 2.1.2.3 Effect of temperature variations 33, URL: https://cds.cern.ch/record/331061.

[5] K. J. Anderson et al., 'Calibration of ATLAS Tile Calorimeter at Electromagnetic Scale', tech. rep. ATL-TILECAL-PUB-2009-001. ATL-COM-TILECAL-2008-016, CERN, 2008, URL: https://cds.cern.ch/record/1139228.

[6] ATLAS Collaboration, *Readiness of the ATLAS Tile Calorimeter for LHC collisions*, Eur. Phys. J. C **70** (2010) 1193, arXiv: 1007.5423 [hep-ex].

[7] C. Fischer, 'Study of TileCal scintillators irradiation using the Minimum Bias integrators', tech. rep. ATL-TILECAL-PROC-2016-006, CERN, 2016, URL: https://cds.cern.ch/record/2160267.

[8] ATLAS Collaboration, *Measurement of $W^{\pm}$ and Z-boson production cross sections in pp collisions at $\sqrt{s}$ = 13 TeV with the ATLAS detector*, Phys. Lett. **B759** (2016) 601, arXiv: 1603.09222 [hep-ex].